Article

Not peer-reviewed version

A Novel Physiologically Based Algorithm (PBA) for Fast CFD Computation of Flow Fractional Reserve (FFR) in Coronary Artery Trees

Sholpan Sumbekova , Xiaohui Su , Yong Zhao *

Posted Date: 16 January 2023

doi: 10.20944/preprints202301.0276.v1

Keywords: FFR; Blood Flow Simulation; SimVascular; coronal stenosis; cCTA

Article

A Novel Physiologically Based Algorithm (PBA) for Fast CFD Computation of Flow Fractional Reserve (FFR) in Coronary Artery Trees

Sholpan Sumbekova [1], Su Xiaohui [2] and Yong Zhao [1]

[1] Mechanical and Aerospace Engineering Department, School of Engineering, Nazarbayev University, Astana 010000, Kazakhstan; sholpan.sumbekova@nu.edu.kz, +7-778-498-00-42

[2] School of Hydraulic Engineering, Dalian University of Technology, China 116024; sxh@dlut.edu.cn, 86-411-84707763

* Correspondence: yong.zhao@nu.edu.kz, +65-8323-3981.

Abstract: A novel physiologically based algorithm (PBA) for fast CFD computation of Flow Fractional Reserve (FFR) in Coronary Artery Trees (CATs) is proposed and developed, which, unlike traditional methods, is based on the extension of the Murray's law for blood vessels at the outlets and extra inlet conditions prescribed alternatively and iteratively. The PBA is then implemented in both SimVascular and Ansys CFD for testing and validation. For validation purpose, 3D models of CATs are built by using their CT images and computational meshes generated for mesh convergence study. Results obtained are then compared with Invasive Coronary Angiographic (ICA) data for validation and evaluation of its accuracy and computational efficiency. It is found that discrepancies between experimental and calculated values of pressure and flow rate at the inlet were less than 0.1% at the end of the 10th round of iteration or less. Further validation shows that the difference between estimated and experimental FFR agree with each other with a maximum difference of 1.62% after convergence is achieved. The PBA is found to be a robust patient-specific and physiologically sound method that can be a good alternative to the existing Lumped Parameter Model (LPM) which is based on empirical scaling correlations using limited population-averaged data and requires nonlinear iterative computation for convergence.

Keywords: FFR; blood flow simulation; SimVascular; coronal stenosis; cCTA

1. Introduction

Coronary arteries are amongst the vital blood vessels which maintain constant blood supply into the heart. Stable blood flow needs to be ensured for the heart to perform normal cardiac functions. A physiologically normally functioning heart can perform 75 cycles per minute on average and sustain continuous blood circulation [1]. The change of coronary artery shape caused by atherosclerosis may result in a reduction of blood flow inside the artery, which in turn, might contribute to the development of abnormal cardiac cycles due to ischemia. The plaque formation on the walls of the coronary arteries increases the possibility of blood flow reduction and may contribute to the progression of coronary artery disease (CAD). According to the World Health Organization Report, in Kazakhstan, 50% of mortality due to the health-related diseases results from CAD [2] and about 2200 American citizens die from CAD-related diseases every day [3].

The accurate diagnosis of the severity of coronary artery stenosis is crucial for the correct treatment of CAD. Hemodynamic and anatomical parameters of the cardiovascular system are used in the evaluation of coronary artery stenosis. The anatomical approach is focused on acquiring geometrical data about the vessels. The diameter of the deviated vessel cross-section and area of the coronary stenosis region is compared to the "normal" region with the absence of plaque formation. This technique involves the application of computed tomography angiography (CTA) which

 doi:10.20944/preprints202301.0276.v1

performs x-ray CT scan of coronary blood vessels. Computer image processing generates geometrical data about the vessels, which enables doctors to identify the vessel obstructions visually. Meijboom et al. [4] have found that Coronary Computed Tomographic angiography (cCTA) for the analysis of CAD often overestimates the clinical severity of geometrical obstructions in coronary vessels, resulting in a true negative rate of 64%.

Hemodynamic parameters describe the motion of blood flow which may be affected by the vessel obstructions. Blood pressure and heart rate are widely used as non-invasive indicators of hemodynamic conditions. Spaan et al. [5] have proposed to use Fractional Flow Reserve (FFR) to describe the hemodynamic condition of the cardiovascular system, which is defined as the ratio of the pressure distal to the stenosis to the pressure proximal to it. FFR can be measured directly during the Invasive Coronary Angiography (ICA) using pressure sensors passing through the guide-catheters and guide-wires [6]. Thus, through this procedure, the difference in pressure values across coronary stenosis regions could be obtained.

Numerous studies have verified the effectiveness of FFR based diagnosis in terms of cost and severity and long-term outcome. For example, Puymirat et al. [7] conducted a clinical study where patients underwent conventional angiography-guided and FFR guided treatments with revascularization. Revascularization is a clinical operation in which plaque formation region of the vessel is enlarged by means of surgical intervention, so that normal blood movement is recovered. The results showed that FFR based treatment had decreased combined death and non-fatal myocardial infarction by 5.46 times compared to conventional angio- revascularization [7]. They also have noted that FFR based treatment is 31% cheaper than conventional angio-treatment. Pijls et al. [8] studied the functional severity assessment of CAD among patients. It was found that the FFR technique could produce 93% accuracy in prediction of reversible ischemia in a study group of 45 patients. De Bruyne et al. [9] suggested that the implementation of FFR guided Percutaneous coronary intervention (PCI) treatment would decrease the rate of urgent revascularization, where a special stent is inserted in a stenosis-containing artery by a surgeon, in order to enlarge the geometrical obstruction of a vessel under the PCI procedure.

The images generated during a CT scan can be used to create three-dimensional (3D) solid models that may be viewed on a monitor, printed on film or by a 3D printer, or to be used by a Computational Fluid Dynamics (CFD) method which allows clinicians to assess quantitatively the coronary physiology within the artery. The existing CFD packages that have been clinically tested in large clinical trials are Discover Flow, HeartFlow - NXT and other Platforms for the physiologic assessment of coronary artery function [11]. The use of CFD to estimate FFR (FFR_{CFD}) has been considered as a promising non-invasive substitute of FFR_{ICA} measurement [11]. Many studies demonstrate that the FFR_{CFD} derived from cCTA through CFD simulations has improved the diagnostic accuracy and discrimination than CT alone for the detection of coronary lesions that cause myocardial ischemia, especially for intermediate stenosis [12], which is also much cheaper and non-invasive, thus much less much harmful to the patients compared with ICA.

However, a coronary tree normally has numerous branches, the outflow boundary conditions become almost impossible to be determined experimentally due to their small sizes. Therefore, the Windkessel-type boundary conditions based on the so-called Lumped Parameter Model (LPM), and the more complicated Lumped Parameter Network Model (LPNM) are normally adopted for approximately calculating the outflow boundary conditions which represent the extremely complex dynamic interactions between the tree and its downstream microvasculature [13,14]. These methods are based on the circuit analogy theory which requires the determination of resistances, capacitances and empirical correlations which are often difficult to calculate without a specific patient's data and are usually not physiologically based. The coupling of the resultant ODEs from these methods with the CFD solver also create ambiguous boundary conditions that may often lead to slow convergence or even divergence in numerical solutions [13,14].

In this study, we propose an efficient PBA for patient-specific calculation of coronary tree outflow boundary conditions to provide a solution to the above-mentioned difficulties, which can provide realistic and personalized outflow boundary conditions in the absence of measured data,

 doi:10.20944/preprints202301.0276.v1

based on an extension of Murray's law and extra inlet conditions [15] to be applied alternatively and iteratively. Vascular systems obey Murray's law, which states that the power for transport and upkeep of blood is minimal in mammalian vascular transport systems, which is employed by the proposed PBA to prescribe the initially boundary conditions, which , in turn, are modified through alternatively applying the extra inlet boundary conditions and iterations towards final numerical convergence.

2. Mathematical Formulations and Numerical Methods

2.1. Governing Equations for Hemodynamic Flow

Simvascular includes a flow solver based on PHASTA (Parallel, Hierarchic, Adaptive, Stabilized, Transient, Analysis) [16], which numerically solve the governing equations for flow in blood vessels. PHASTA is a parallel unstructured grid solver to calculate 3D compressible and incompressible, laminar and turbulent, steady and unsteady flows. Incompressible 3D Navier-Stokes equations (1) are used to solve blood flow in SimVascular:

$$\rho\dot{v}_i + \rho v_j v_{i,j} - p_{,i} - \tau_{ij,j} = 0,$$
$$v_{i,i} = 0, \quad (1)$$

ρ – density of blood
v_i – i component of flow velocity
$\dot{v}_i$ – velocity derivative with respect to time
p – pressure
τ_{ij} – stress tensor (viscous portion)

Streamline-upwind/Petrov-Galerkin (SUPG) and pressure-stabilizing/Petrov-Galerkin (PSPG) Finite Element Methods are used to discretize the Navier-Stokes equation (1) in space and are integrated in time by an implicit scheme. The resultant algebraic equations are solved bv a so-called preconditioned linear solver (PCLS) [16].

On the other hand, the Ansys CFX solver solves the same Navier-Stokes equations with the Finite Volume Method (FVM) and SIMPLE/SIMPLEC/PISO pressure correction methods for impressible flows [18].

Domain of equation is defined with $\Omega \in \mathbb{R}^3$, and boundary condition are $\Gamma = \Gamma_D \cup \Gamma_N$, where Γ_D is Dirichlet Boundary Condition (BC) and Γ_N Neumann BC. The discretization of Ω is performed with n_{el} linear unstructured tetrahedral elements, $\bar{\Omega}_e$. At the end, eq (1) is transformed into eq (2):

$$B_G(w_i, q; v_i, p) = \int_\Omega \{w_i(\rho\dot{v}_i + \rho v_j v_{i,j}) + w_{i,j}(-\rho\sigma_{ij} + \tau_{ij}) - q_{,i}v_i\}d\Omega +$$
$$\int_{\Gamma_N}\{w_i(\rho\delta_{in} + \tau_{in}) + qv_{in}\}d\Gamma \quad (2)$$

where $w \in W_n^k$ *and* $q \in P_h^k$

2.2. The Murray's Law and PBA for Rapid Iterative Computation of Outlet Conditions

The methodology proposed in this study aims to provide a solution to the above-mentioned difficulties with Windkessel type boundary conditions, and generate patient-specific realistic outflow boundary conditions in the absence of measured data, based on an extension of the Murray's law [15] and extra inlet conditions prescribed alternatively in iterations. Vascular systems are found to obey Murray's law, which states that the power for transport and upkeep of blood is minimal in a vascular transport system.

According to the Hagen-Poiseuille Law for laminar flow in a vessel, the power required to drive a blood flow through it is

$$P_t = \frac{8\mu l}{\pi r^4}\dot{Q}^2 \quad (3)$$

where $\dot{Q}$ is the volumetric flow rate, l the length of the vessel, r its radius and μ the blood viscosity.

 doi:10.20944/preprints202301.0276.v1

Furthermore, the power necessary for the maintenance of the blood in the vessel is proportional to the blood volume in the vessel:

$$V = \pi l r^2 \tag{4}$$

The power required to maintain the metabolism in the blood is thus

$$P_m = \lambda V = \lambda \pi l r^2 \tag{5}$$

where λ is the metabolic rate of the blood.

The total power required to drive the blood and maintain it is

$$P = P_t + P_m = \frac{8\mu l}{\pi r^4}\dot{Q}^2 + \lambda \pi l r^2 \tag{6}$$

The radius that meets the minimum power requirement is obtained through the differentiation of P with respect to r and setting it to zero:

$$\frac{dP}{dr} = -\frac{32\mu l}{\pi r^5}\dot{Q}^2 + 2\lambda \pi l r = 0 \tag{7}$$

Thus

$$\dot{Q} = \frac{\pi}{4} r^3 \sqrt{\frac{\lambda}{\mu}} \tag{8}$$

This functional relationship exists between vessel radius and volumetric flow rate in individual vessels. A novel iterative scheme is thus proposed to couple the Murray's law with CFD simulation to search for the converged patient-specific flow outlet conditions for all the outlets of a coronary tree for given inlet pressure and volumetric flow rate which are prescribed alternatively through iterative computation.

For a particular branch i of a coronary tree with N branches as shown in Figure 1, its outflow is

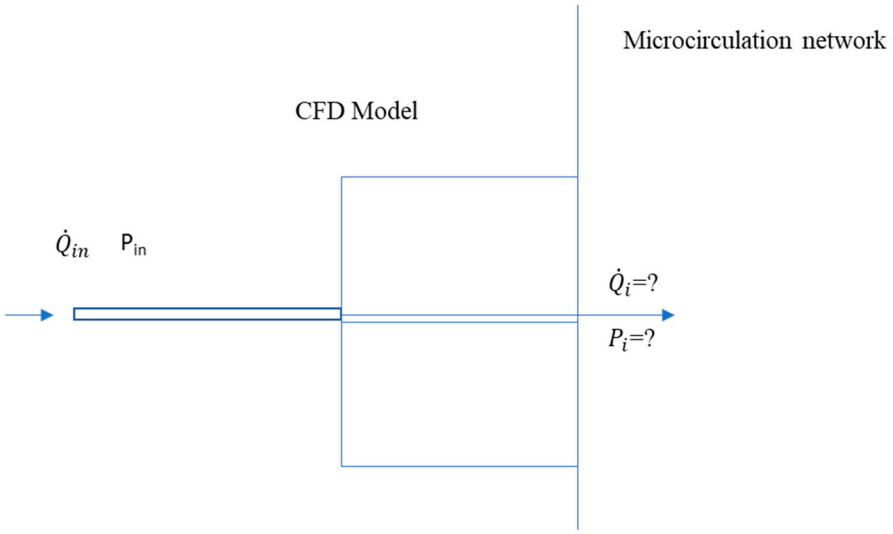

Figure 1. Schematic of the new boundary model.

$$\dot{Q}_i = \frac{\pi}{4} r_i^3 \sqrt{\frac{\lambda}{\mu}} \tag{9}$$

And according to the conservation law, we have

$$\dot{Q}_{in} = \sum_{i=1}^{N} \dot{Q}_i \tag{10}$$

$$\dot{Q}_i = \frac{r_i^3}{r_{in}^3}\dot{Q}_{in} \tag{11}$$

Our new physiologically based algorithm (PBA) to extract personalized/patient-specific outflow boundary conditions that represent the interactions between the coronary tree and its micro circulation network downstream under both steady and unsteady conditions are shown in a flowchart as illustrated in Figure 2.

Preprints.org (www.preprints.org) | NOT PEER-REVIEWED | Posted: 16 January 2023 doi:10.20944/preprints202301.0276.v1

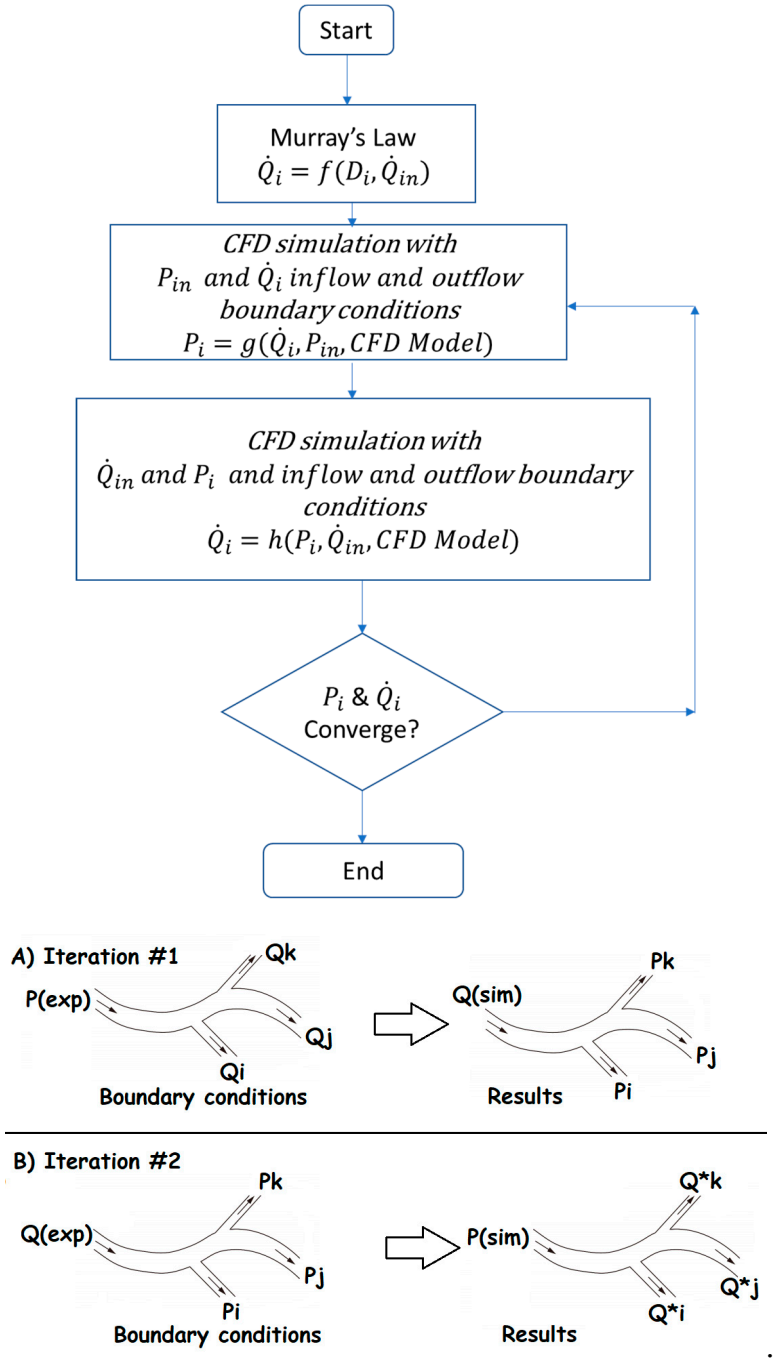

Figure 2. Algorithm for the outflow boundary conditions.

In this work the above-mentioned methods are implemented in both SimVascular and Ansys CFX to perform computational study of the hemodynamics in a number of patient specific geometries with the aim of validating the methods using related ICA measurements, such as inlet flow rate and pressure and FFR_{ICA}. There are four vascular cases, named as CT209, CT14, CHN03 and CHN13 implemented by using the proposed PBA. Table 1 lists the workflow procedure for the PBA.

Table 1. Workflow procedure of Rapid Iterative algorithm.

		Inlet	Outlets			
1st round of iteration	Input to CFD Solver	P_{exp}[a]	Q_1	Q_2	…	Q_n
		*calculated by Murray's law at beginning				
	The output from CFD Solver	Q_{ss}	P_1^{ss}	P_2^{ss}	…	P_n^{ss}
	Input to CFD solver	Q_{exp}[b]	P_1^{ss}	P_2^{ss}	…	P_n^{ss}

Preprints.org (www.preprints.org) | NOT PEER-REVIEWED | Posted: 16 January 2023 doi:10.20944/preprints202301.0276.v1

	Output from CFD Solver	P_{ss}	Q_1^{ss}	Q_2^{ss}	…	Q_n^{ss}
	Input to CFD solver	P_{exp}	Q_1^{ss}	Q_2^{ss}	…	Q_n^{ss}
2nd round of iteration	Output from CFD solver	Q_{ss}	P_1^{ss}	P_2^{ss}	…	P_n^{ss}
	Input to CFD solver	Q_{exp}	P_1^{ss}	P_2^{ss}	…	P_n^{ss}
	Output from CFD solver	P_{ss}	Q_1^{ss}	Q_2^{ss}	…	Q_n^{ss}
Nth round of iteration	-	-	-	-	-	-

[a] Experimentally measured distal pressure at the inlet of blood vessel. [b] Experimentally measured flow rate at the inlet of blood vessel.

$Q_{ss}; P_{ss}; Q_n^{ss}; P_n^{ss}$ – CFD solver calculated values of pressure and flow rate at the inlet and outlets at different stages.

The geometries and their outlets of CT209 and CHN13 are presented in Figures 3 and 4, while Figures 5 and 6 show the geometries and outlets of CT14 and CHN03, respectively.

Tables 2–5 show the experimental values of pressure and flow rate at the inlet (aorta) of a vessel that is obtained for CT209, CHN13, CT14 and CHN03, respectively, while Tables 6–9 show the calculated initial flow rates at the outlets for the four models, which are calculated using equation (11) which is based on Murray's law. Inlet and outlet boundary conditions are prescribed according to Table 1.

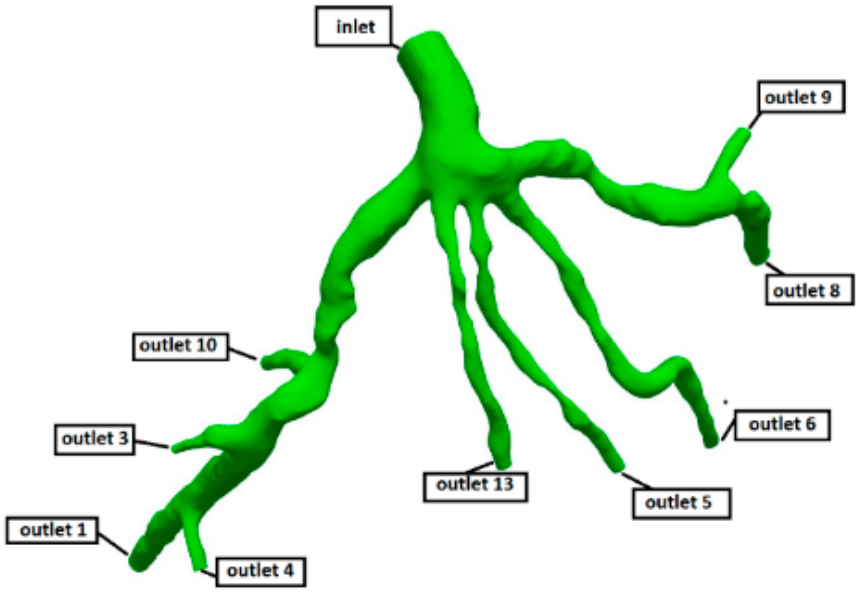

Figure 3. Geometry and Outlets of the CT209 model.

Preprints.org (www.preprints.org) | NOT PEER-REVIEWED | Posted: 16 January 2023 doi:10.20944/preprints202301.0276.v1

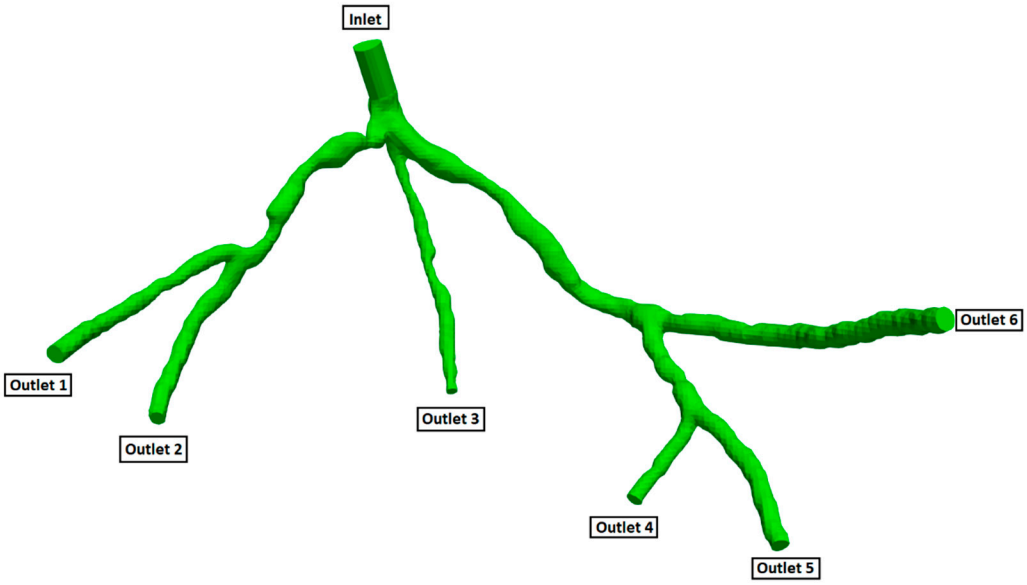

Figure 4. Geometry and Outlets of the CHN13 model.

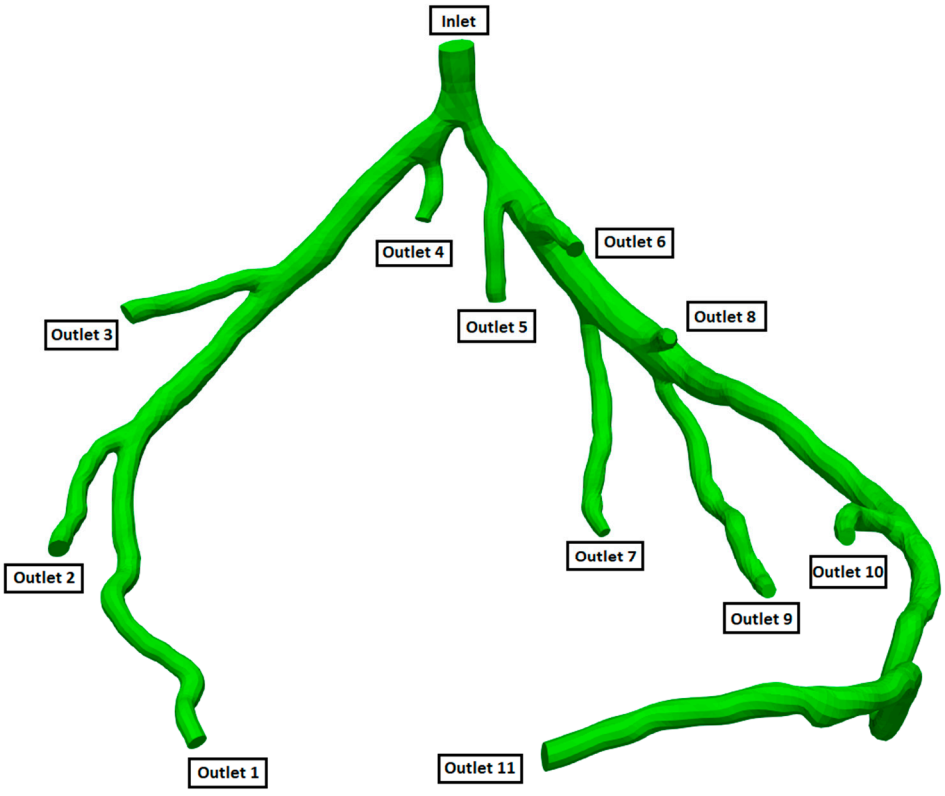

Figure 5. Geometry and Outlets of the CT14 model.

Preprints.org (www.preprints.org) | NOT PEER-REVIEWED | Posted: 16 January 2023 doi:10.20944/preprints202301.0276.v1

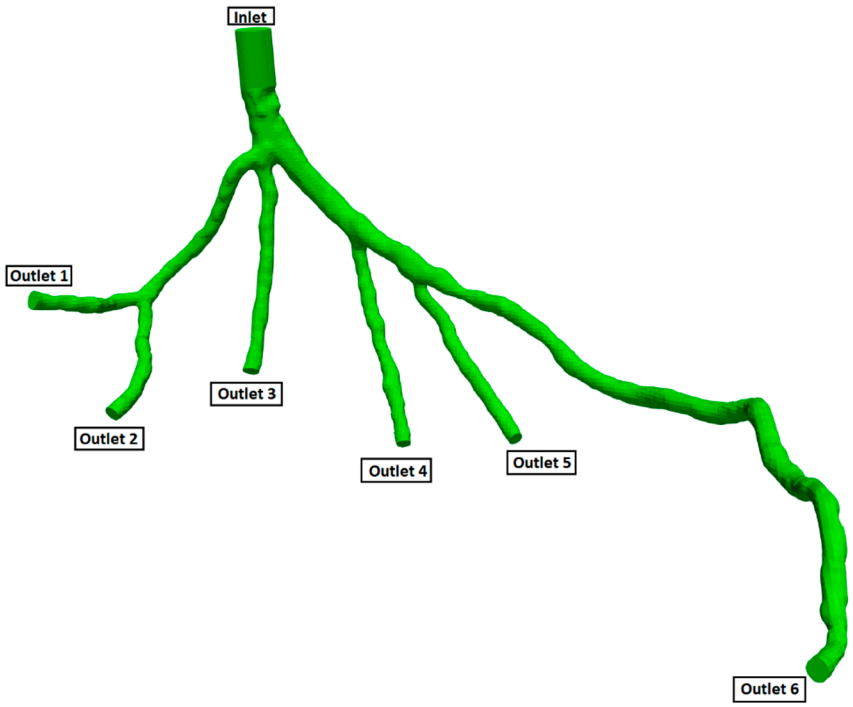

Figure 6. Geometry and Outlets of the CHN03 model.

Table 2. Experimentally obtained input parameters for simulation for CT209.

Parameter	Value
Experimental inlet pressure P_{exp}	90.53 mm Hg (12070.12 Pa)
Experimental inlet flow rate Q_{exp}	9.39944 cm³/s

Table 3. Experimentally obtained input parameters for simulation for CHN13.

Parameter	Value
Experimental inlet pressure P_{exp}	90.61 mm Hg (12870.12 Pa)
Experimental inlet flow rate Q_{exp}	7.17551 cm³/s

Table 4. Experimentally obtained input parameters for simulation for CT14.

Parameter	Value
Experimental inlet pressure P_{exp}	76.8 mm Hg (10240.8 Pa)
Experimental inlet flow rate Q_{exp}	6.19 cm³/s

Table 5. Experimentally obtained input parameters for simulation for CHN03.

Parameter	Value
Experimental inlet pressure P_{exp}	76.5 mm Hg (10201.9 Pa)
Experimental inlet flow rate Q_{exp}	6.18 cm³/s

Table 6. Initial calculated flow rates at each outlet by Murray's law for CT209.

Murray's law calculation for outlet flow rates						
	i	A_i (cm²)	d_i (cm)	d_i^3 (cm³)	α_i	Q_i (cm³/s)
outlet 1	1	4.114	2.289	11.988	0.315	2.965
outlet 3	2	0.568	0.851	0.616	0.016	0.152
outlet 4	3	0.925	1.085	1.279	0.034	0.316
outlet 5	4	0.977	1.116	1.388	0.037	0.343
outlet 6	5	1.802	1.515	3.475	0.091	0.859

outlet 8	6	4.105	2.286	11.948	0.314	2.955
outlet 9	7	1.674	1.460	3.111	0.082	0.769
outlet 10	8	1.173	1.222	1.824	0.048	0.451
outlet 13	9	1.398	1.334	2.374	0.062	0.587

Table 7. Initial calculated flow rates at each outlet by Murray's law for CHN13.

Murray's law calculation for outlet flow rates						
	i	A_i (cm²)	d_i (cm)	d_i^3 (cm³)	α_i	Q_i (cm³/s)
outlet 1	6	2.712	1.858	6.418	0.227	1.630
outlet 2	1	1.832	1.527	3.564	0.126	0.905
outlet 3	3	1.005	1.131	1.447	0.051	0.368
outlet 4	2	1.950	1.576	3.913	0.139	0.994
outlet 5	5	1.969	1.583	3.970	0.141	1.009
outlet 6	4	3.382	2.075	8.936	0.316	2.270

Table 8. Initial calculated flow rates at each outlet by Murray's law for CT14.

Murray's law calculation for outlet flow rates						
	i	A_i (cm²)	d_i (cm)	d_i^3 (cm³)	α_i	Q_i (cm³/s)
outlet 1	1	2.0253	1.6058	4.1410	0.1008	0.6238
outlet 2	2	2.5091	1.7874	5.7102	0.1390	0.8602
outlet 3	3	2.8210	1.8952	6.8072	0.1657	1.0254
outlet 4	4	1.8029	1.5151	3.4779	0.0846	0.5239
outlet 5	5	1.9039	1.5570	3.7744	0.0919	0.5686
outlet 6	6	2.2769	1.7026	4.9359	0.1201	0.7436
outlet 7	7	1.2534	1.2633	2.0160	0.0491	0.3037
outlet 8	8	1.0056	1.1315	1.4487	0.0353	0.2182
outlet 9	9	1.2546	1.2639	2.0189	0.0491	0.3041
outlet 10	10	1.3891	1.3299	2.3522	0.0572	0.3543
outlet 11	11	2.11181	1.6398	4.4091	0.1073	0.6642

Table 9. Initial calculated flow rates at each outlet by Murray's law for CHN03.

Murray's law calculation for outlet flow rates						
	i	A_i (cm²)	d_i (cm)	d_i^3 (cm³)	α_i	Q_i (cm³/s)
outlet 1	1	2.5675	1.8081	5.9106	0.2240	1.3847
outlet 2	2	2.2262	1.6836	4.7721	0.1808	1.1179
outlet 3	3	2.1930	1.6710	4.6658	0.1768	1.0930
outlet 4	4	1.8206	1.5225	3.5293	0.1338	0.8268
outlet 5	5	1.7784	1.5048	3.4074	0.1291	0.7982
outlet 6	6	2.0126	1.6008	4.1021	0.1555	0.9610

The convergence criteria is evaluated at the end of each iteration with equation (12). The procedure presented in Table 1 is repeated continuously until the convergence is achieved.

$$\frac{|P_{ss}-P_{exp}|}{P_{exp}} = \delta \leq 0.1\% \quad (12)$$

$$\Delta P = \frac{|P_{calculated}-P_{experimental}|}{P_{calculated}} \times 100\% \quad (13)$$

$$\Delta Q = \frac{|Q_{calculated}-Q_{experimental}|}{Q_{calculated}} \times 100\% \quad (14)$$

$$FFR = \frac{\min\left(P_1^{SS}, P_2^{SS}, \ldots P_n^{SS}\right)}{P_{exp}} \quad (15)$$

 doi:10.20944/preprints202301.0276.v1

3. Results and Discussion

Mesh generation is performed using the open source TetGen kernel and MeshSim, which generate volumetric meshes in the blood vessels. In particular, TetGen is capable of generating tetrahedral meshes for a diverse variety of geometries automatically. Ansys MESH, a commercial software, is used to generate meshes for simulations using Ansys CFX.

Estimated minimum mesh size for each mesh is about a half of the radius of the smallest artery (inlet/outlet) present in the model. Estimated mesh size for the coronary artery tree model CT209 (as shown in Figure 3) is 0.1702, and for CHN13 it is 0.2262. Tables 10 and 11 show the statistics of generated meshes. Mesh refinement has resulted in a larger number of mesh elements without the expansion layers near the vessel walls, which are difficult to implement due to the complexity of the geometries, which in turn increase the computational time for each simulation. For example, a decrease of mesh size from 0.20 to 0.1702 has resulted in 1.7 times increase in computational time.

The convergence criteria of $\frac{|P_{ss}-P_{exp}|}{P_{exp}} = \delta \leq 0.1\%$ for inlet pressure, defined in equation (12), is used for all computations.

There are four sets of meshes generated for CT14 (with mesh cell numbers as: 118,874, 231,930, 486,447, 1,052,529) and five sets of meshes for CHN03 (with mesh element numbers as: 69,681, 139,833, 286,897, 406,606, 779,482) to study mesh convergence. The results are shown in Figures 7 and 8. Figure 7 shows that when the grid number is increased from 100,000 to about 1.05 million, the change value of the distal pressure is less than 5% (about 2.2%). After mesh dependency test, the model was discretized with a total of about 0.5 million volume cells. Further grid refinement leads to < 1% relative error. For case CHN03, the mesh convergent results are shown in Figure 8. The number of volume cells was set to 0.4 million at last.

For CT209, the relative difference between experimental and computed values of inlet pressure and inlet flow values are plotted in Figures 9 and 10, respectively. The relative percentage differences of calculated and experimentally measured (ICA) pressure and flow rate are obtained using equations (13) and (14). The overall trend shows that with more iterations, the relative difference values for pressure and flow rate decrease steadily for all four mesh sizes. Relative flow rate difference appears to be less than 0.04% for all iterations. The relative difference value for pressure for the mesh size of 0.1702 has dropped from 0.79% in the second iteration to 0.21% in the tenth iteration. However, for the mesh size of 0.20, relative pressure difference has decreased from 0.5% in the fourth round of iteration to 0.001% in the twelfth iteration.

Pressure and velocity residuals at all the outlets are defined as the averages of relative percentage differences in consecutive iterations. The convergence of CFD simulation can be monitored by examining the reduction of the values of the pressure and flow rate residuals at the outlets as well. Figures 11 and 12 show pressure and flow rate residuals at the outlets for CT209, respectively, for all iterations where residual values are plotted in logarithmic scale. Mesh sizes of 0.1702 and 0.20 have the same fluctuation behaviors for all round of iterations. Minimum pressure residual values of 1.93E-7 and 2E-7 are observed for both meshes, whereas the maximum values are 3.62E-7 and 4.43E-7 respectively. It is important to note, that the mesh sizes of 0.24 and 0.26 show a different trend of fluctuations. The values of pressure residual fluctuate from 1.30 E-7 to 3.03E-7 in each consecutive simulation, i.e., in each round of iteration. In addition, greater magnitudes of residual fluctuations are observed in Figures 11 and 12 for the mesh sizes of 0.24 and 0.26. For example, flow rate residual of 6.75E-6 is observed in the first iteration and it increases up to 2.72E-4 in the second one. However, finer meshes with the mesh sizes of 0.20 and 0.1702 do not show such an increase in flow rate residuals for each consecutive iteration.

FFR is calculated using equation (15). The experimental value of FFR is 0.76 for CT209 model [16]. Figures 13 and 14 show the obtained values of FFR at each round of iteration and the percentage relative difference of calculated and experimental FFR (degree of deviation from experimentally obtained FFR). The results obtained from 0.1702 and 0.20 mesh sizes are very close to the experimental value of FFR=0.76 at the end of the eighth and the tenth round of iteration, respectively. At the same time, the results obtained from 0.24 and 0.26 mesh sizes demonstrate a constant decrease

 doi:10.20944/preprints202301.0276.v1

in Figure 13, which yield a constant negative slope. FFR values for mesh sizes of 0.1702 and 0.20 have converged when they have reached the experimental FFR value. The percentage relative difference of FFR values of 0.20% and 0.34% are recorded for the mesh sizes of 0.1702 and 0.20, respectively. Zhang et al. [17] have computed non-invasive FFR value of 0.73 whereas experimental (ICA) FFR is about 0.76 for CT209 model. The final values of FFR for mesh sizes of 0.1702 and 0.20 are FFR=0.758 and FFR=0.757 which agree very well with the ICA FRR.

The location of Left Anterior Descending (LAD) Proximal artery is indicated as artery stenosis region for CT209 model in Zhang et al. [17]. The dark blue region of the blood vessel is LAD Proximal in Figure 15. Therefore, it is found that the artery stenosis is located in the same region as it was observed by Zhang et al. [17]. Figure 15 presents the visualized results of FFR at the end of the tenth iteration for the mesh size of 0.1702. The visualization of velocity streamlines is presented in Figure 16, where it can be observed that there is an increase in velocity magnitude in the stenotic region and several possible stenosis are also identified in the figure based on velocity magnitudes.

Table 10. Mesh information for CT209 Model.

Mesh size (mm)	Number of cells	Number of points
0.1702	3,949,528	674,346
0.2000	2,427,621	421,477
0.2400	1,400,809	248,645
0.2600	1,100,097	197,318

Table 11. Mesh information for CHN13 Model.

Mesh size (mm)	Number of cells	Number of points
0.22	1,166,473	211,638
0.35	286,803	57,015
0.53	80,093	18,104

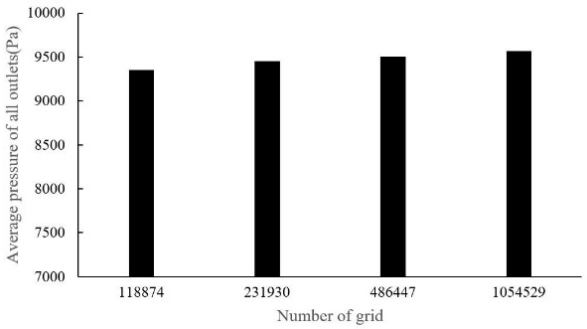

Figure 7. Dependency analysis for CT14.

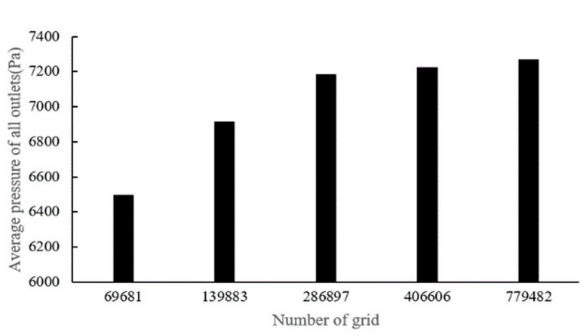

Figure 8. Dependency analysis for CHN03.

Preprints.org (www.preprints.org) | NOT PEER-REVIEWED | Posted: 16 January 2023 doi:10.20944/preprints202301.0276.v1

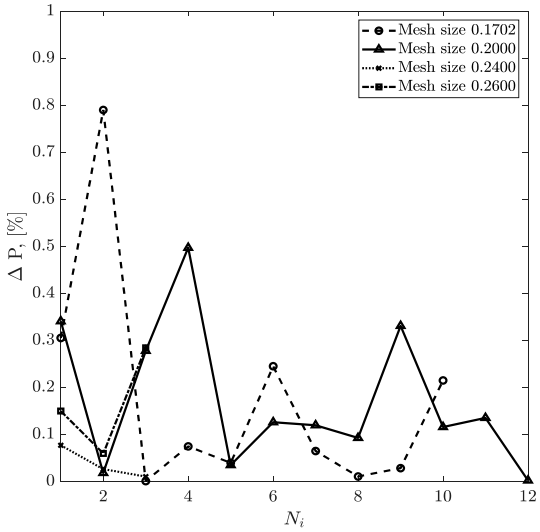

Figure **9.** Inlet pressure relative percentage deviation from the experimental value vs No. of iterations for CT209.

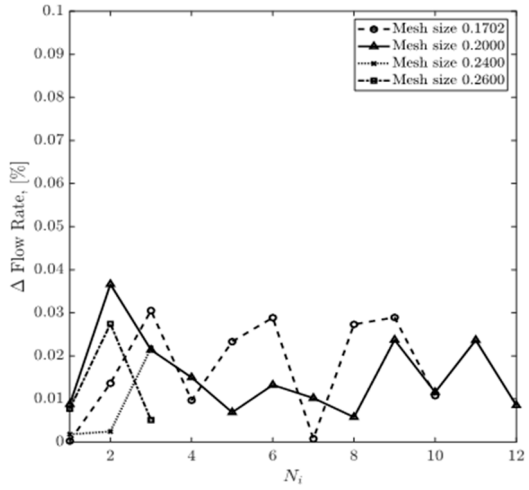

Figure 10. Inlet flow rate relative percentage deviation from the experimental value vs No. of iterations for CT209.

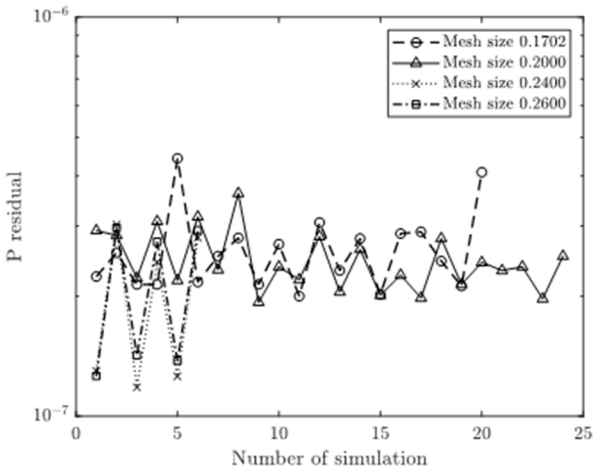

Figure 11. Outlet pressure residual vs No. of iterations for CT209.

Preprints.org (www.preprints.org) | NOT PEER-REVIEWED | Posted: 16 January 2023 doi:10.20944/preprints202301.0276.v1

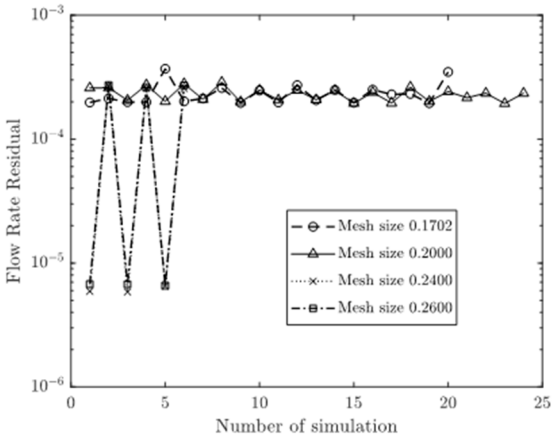

Figure 12. Outlet flow rate residual vs No. of iterations for CT209.

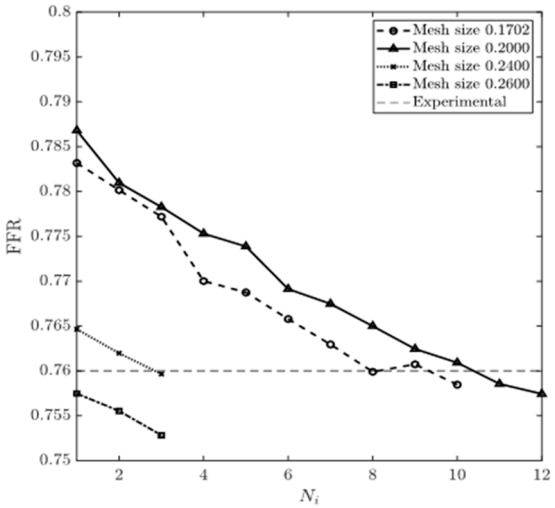

Figure 13. FFR values in each round of iteration for CT209.

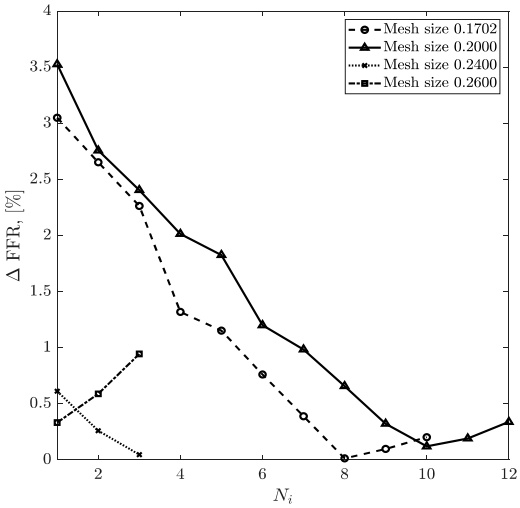

Figure 14. Relative differences between calculated and experimental FFR in each round of iteration for CT209.

Preprints.org (www.preprints.org) | NOT PEER-REVIEWED | Posted: 16 January 2023 doi:10.20944/preprints202301.0276.v1

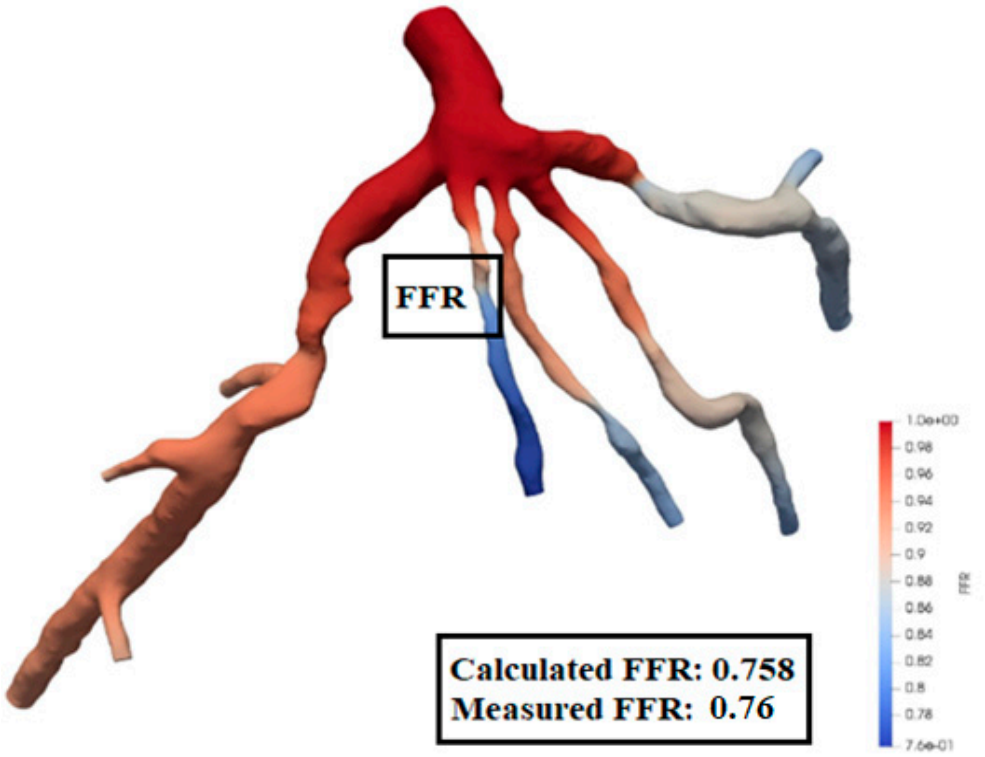

Figure 15. FFR distribution along with the shape of CT209 model.

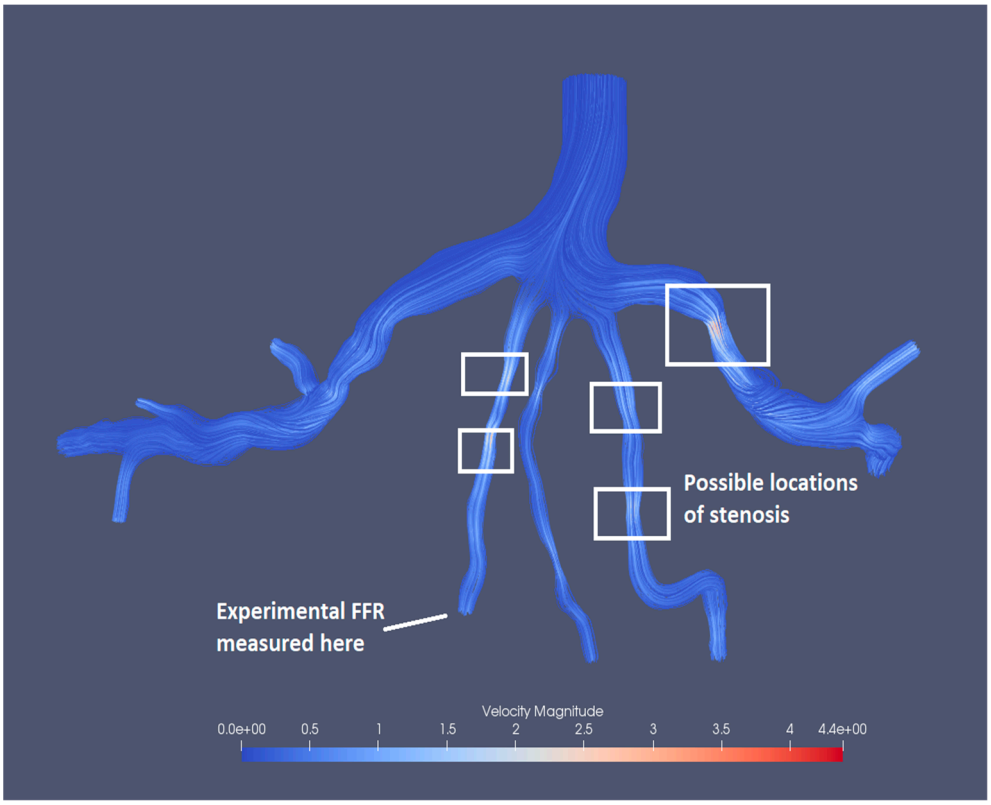

Figure 16. Visualization of velocity streamlines in the CT 209 model.

The simulations of blood flow in the model CHN13 are performed using three mesh sizes (coarse, fine and very fine). Initially, the number of iterations is set to ten, however, since the relative errors for some mesh sizes show systematic increases, the simulations with 0.53 and 0.22 mesh sizes are stopped at the fifth and sixth rounds of iterations, respectively. The relative inlet pressure

 doi:10.20944/preprints202301.0276.v1

differences from the corresponding measurements calculated for the three meshes demonstrate that the maximum pressure difference is less than 1% for all cases, and at the same time, the relative inlet pressure difference is minimum for the mesh size of 0.22 as shown in Figure 17. The relative differences of inlet flow rates for all three mesh sizes are less than 1% with a maximum of 0.02% observed for the finest mesh (see Figure 18). The pressure and flow rate residuals at the outlets for CHN13 are shown in Figures 19 and 20, which fluctuate for all three mesh sizes. The most significant fluctuation is observed for pressure residual with the mesh size of 0.53 (from 5.91*10-8 to 8.95*10-5) and for flow rate residual with 0.35 in mesh size (from 1.7*10-6 to 1.71*10-4). Interestingly the finest mesh size has relatively low pressure residuals (in the interval from 4.02*10-8 to 3.32*10-7) and high flow rate residuals (from 2.33*10-5 to 2.03*10-4). The experimental FFR for the CHN13 model is 0.68. The results show that the finest mesh size (0.22) produces the closest to this value. FFR obtained from the simulations with the finest mesh size is equal to 0.691 as shown in Figure 21. The final values of FFR obtained using 0.35 and 0.53 mesh sizes are 0.619 and 0.531, respectively. Additionally, the results in Figure 22 show that the accuracy of the FFR obtained from simulations with 0.35 in mesh size decreases with the number of iterations. Consequently, the maximum error is observed in the tenth round of iterations. Figure 23 shows a significant decrease in FFR at the location of stenosis caused by pressure drop. The velocity streamlines are presented in Figure 24. The color of the streamlines at the stenosis indicates an increase in velocity.

Figure 25 shows the comparison between the results obtained by traditional lumped parameter method and those obtained by the current method as well as the ICA measurement. It is found that the current method demonstrates better accuracy and efficiency than the traditional methods. Figures 26 and 27 present the visualized pressure distributions for the models CT14 and CHN03, respectively. The calculated FFRs for CT14 and CHN03 by the PBA are 0,975 and 0.691 as shown in Figures 21–27, which have excellent agreement with the corresponding experimental values of 0.97 and 0. 68 respectively. The visualizations of velocity streamlines are represented in Figures 28 and 29.

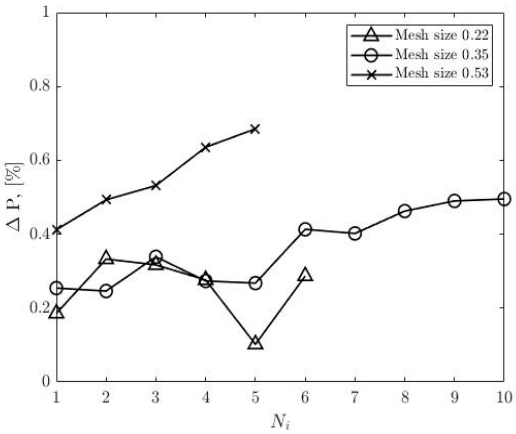

Figure 17. Inlet pressure relative percentage deviation from the experimental value vs No. of iterations for CHN13

Preprints.org (www.preprints.org) | NOT PEER-REVIEWED | Posted: 16 January 2023 doi:10.20944/preprints202301.0276.v1

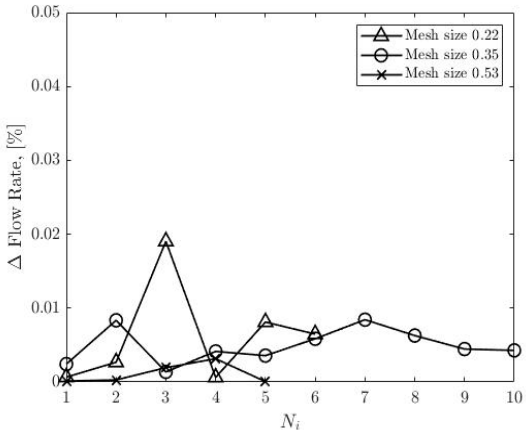

Figure 18. Inlet flow rate relative percentage deviation from the experimental value vs No. of iterations for CHN13.

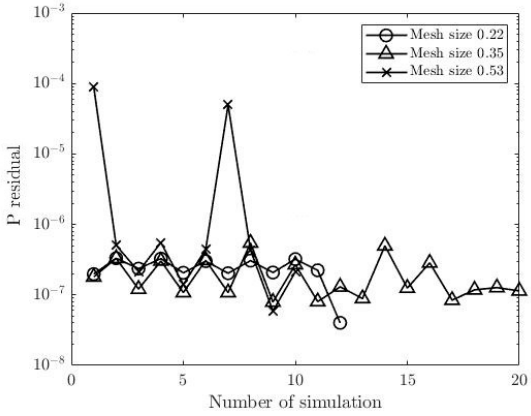

Figure 19. Outlet pressure residual vs No. of iterations for CHN13.

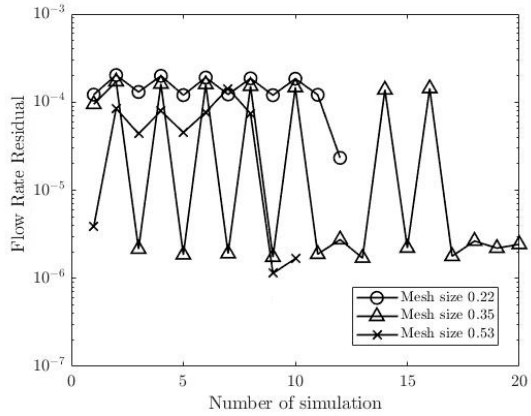

Figure 20. Outlet flow rate residual vs No. of iterations for CHN13.

Preprints.org (www.preprints.org) | NOT PEER-REVIEWED | Posted: 16 January 2023 doi:10.20944/preprints202301.0276.v1

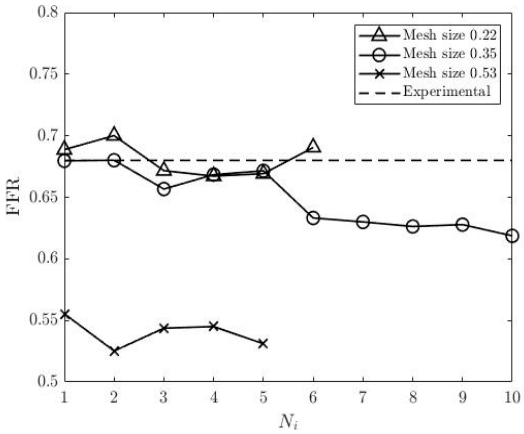

Figure 21. FFR values in each round of iteration for CHN13.

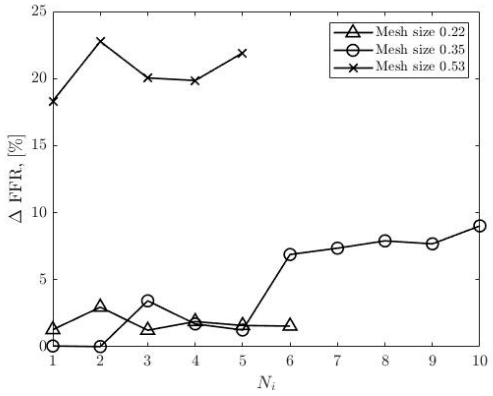

Figure 22. Relative differences between calculated and experimental FFR in each round of iteration for CHN13.

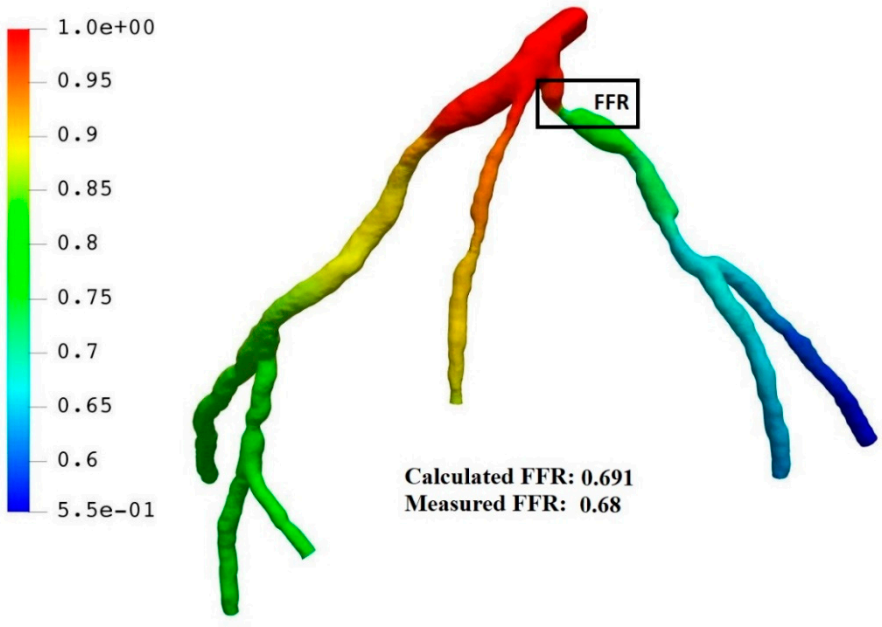

Figure 23. FFR distribution along with the shape of CHN13 model.

 doi:10.20944/preprints202301.0276.v1

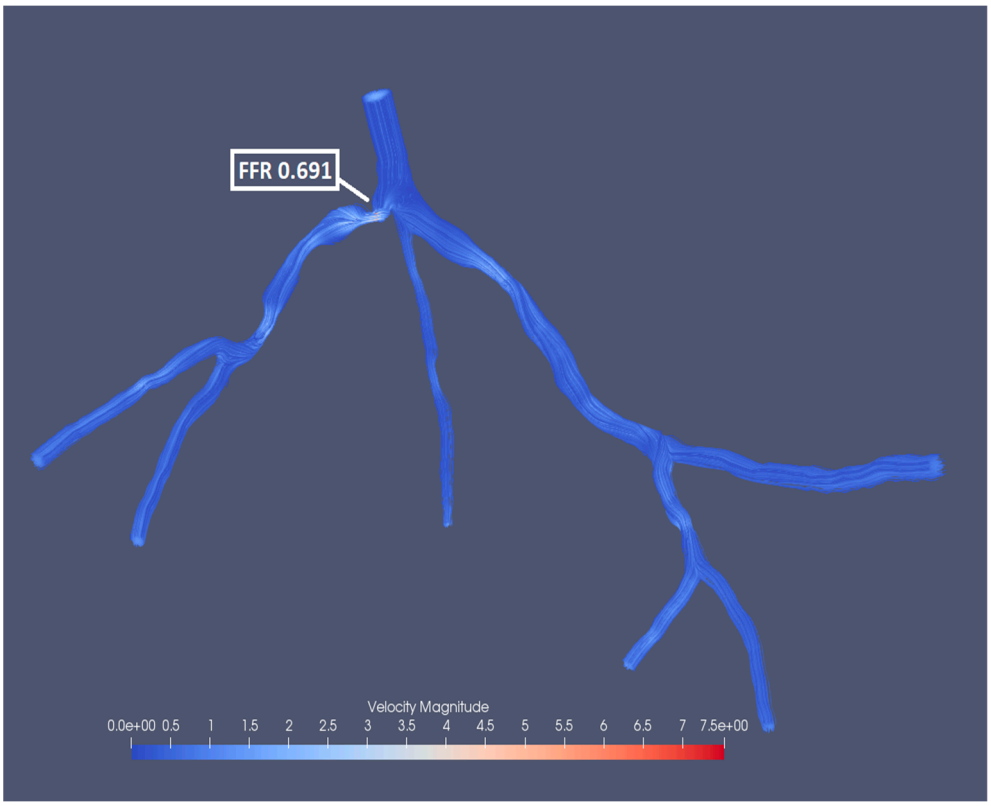

Figure 24. Visualization of velocity streamlines in the CHN13 model.

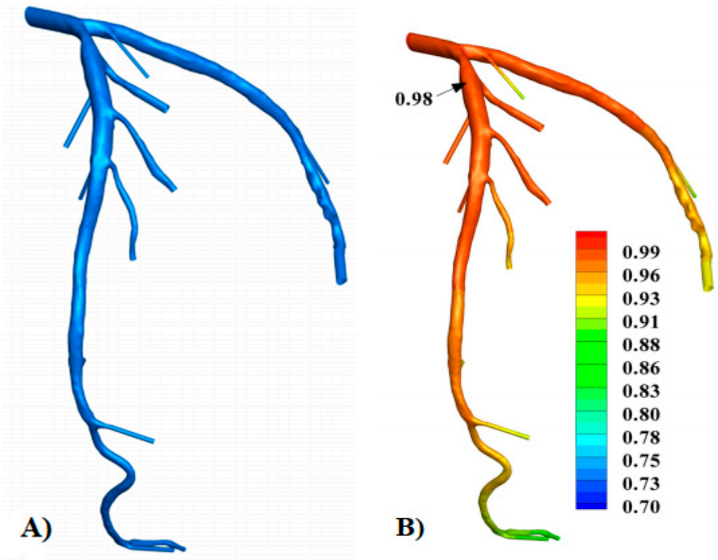

Preprints.org (www.preprints.org) | NOT PEER-REVIEWED | Posted: 16 January 2023 doi:10.20944/preprints202301.0276.v1

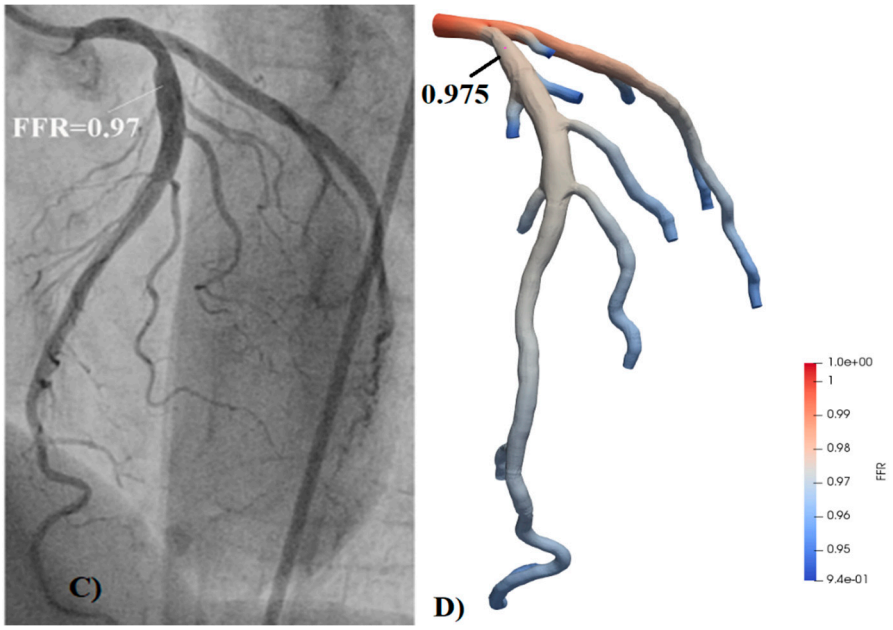

Figure 25. Validation of FFR obtained using PBA with CT14: A) 3D Model of a coronary artery tree; B) FFR obtained from traditional lumped parameter method; C) FFR obtained from ICA; D) FFR obtained using the proposed PBA.

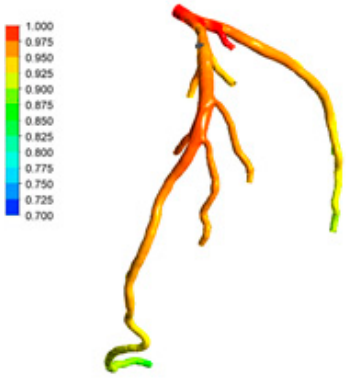

Figure 26. Pressure distributions on CT14

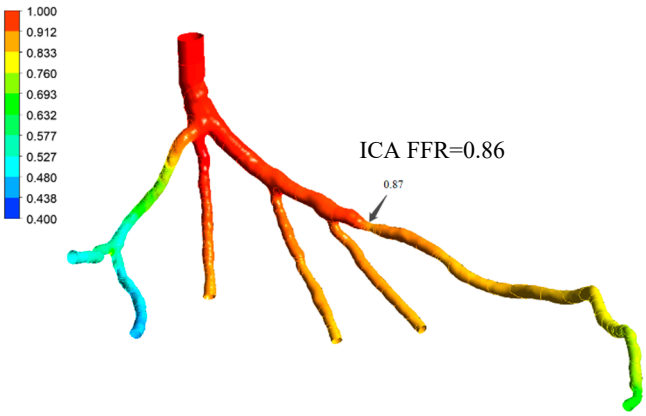

Figure 27. Pressure distributions on CHN03

 doi:10.20944/preprints202301.0276.v1

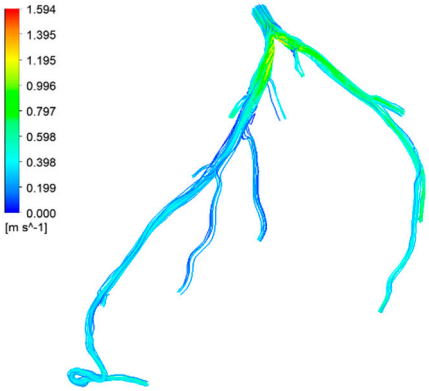

Figure 28. Visualization of velocity streamlines in CHN03

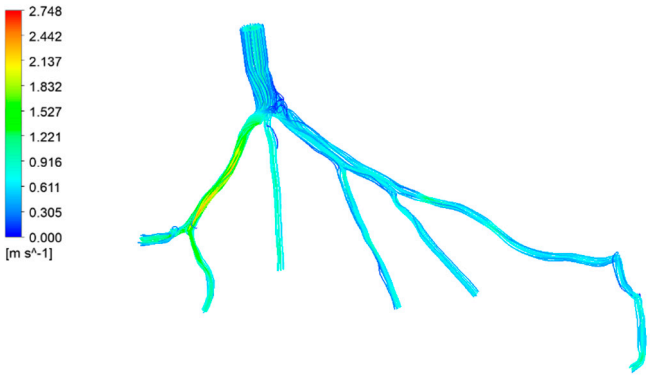

Figure 29. Visualization of velocity streamlines in CT14

Finally a summary of the comparison of the calculated and experimental ICA FFRs are presented in the Table 12. The results show that the differences between the relative errors for Ansys and Simvascular is at most of 3.24%. This shows that the proposed PBA produces results that are solver independent.

Table 12. Relative errors calculated between the invasive and calculated FFRs by both Simvascular and Ansys CFX.

model	Calculated FFR		Invasive FFR	Relative error, %	
	Ansys CFX	Simvascular		Ansys CFX	Simvascular
CT209	0.753	0.758	0.76	0.92	0.26
CT14	0.96	0.97	0.975	1.54	0.51
CHN03	0.87	0.872	0.86	1.16	1.40
CHN13	0.658	0.691	0.68	3.24	1.62

Further validation of the PBA method is performed using traditional LPM method described in the paper by Zhang et al [17] for model CT14. The LPM method uses a reference pressure, resistances at every outlet representing the flow resistance from the downstream microvasculature, an overall resistance for the whole CAT which is related to the outlet resistances through an population-averaged empirical scaling law [17], and an iterative procedure to calculate the resistances and reference pressure, thus resulting in the outlet pressures in each branch outlet. Three simulations were run for the model CT14 using both methods: the traditional LPM method is run using Ansys, while the proposed PBA is used in Simvascular. Table 13 compares the flow rates at the outlets, which show that the percentage deviations between the flow rates obtained using PBA and LPM are below 0.1%, yielding on average 0.036%.

 doi:10.20944/preprints202301.0276.v1

It is found that the LPM cannot always guarantee convergence to a unique solution for every case, while the proposed PBA can generate convergence to accurate solutions for all the four cases studied. This shows that the PBA is far more robust than the LPM because the former is physiologically based and patient specific while the latter is not!

Table 13. The values of flow rate in each branch of the model CT14 calculated using traditional RCR method and novel PBA method.

Outlet	Q_i(RCR)	Q_i(PBA)	Difference, %
outlet 1	0.6224	0.6224	0.0042
outlet 2	0.8534	0.8535	0.0175
outlet 3	1.0260	1.0260	0.0066
outlet 4	0.5205	0.5200	0.1005
outlet 5	0.5733	0.5734	0.0023
outlet 6	0.7437	0.7431	0.0827
outlet 7	0.3051	0.3050	0.0275
outlet 8	0.2200	0.2199	0.0559
outlet 9	0.3077	0.3076	0.0143
outlet 10	0.3560	0.3559	0.0233
outlet 11	0.6623	0.6627	0.0566

4. Conclusion

In this study, blood flow has been simulated in four coronary artery tree models using a proposed physiologically based algorithm (PBA) implemented in both Simvascular and Ansys CFX CFD solvers, in order to evaluate the performance of the PBA in different CFD solvers.. The boundary conditions at the outlets are obtained with the proposed approach based on Murray's law with excess inlet conditions prescribed alternatively and interactively. Mesh convergence studies are conducted to investigate the sensitivity of the method to the change in mesh sizes. The simulations provided accurate values of FFR both by Simvascular and Ansys CFX. The values of FFR obtained from the simulations using the proposed PBA agree very well with the experimental ICA results [17]. The validation and comparison of the traditional and proposed methods show a flow rate relative difference of 0.1% at most. Compared with the traditional method that may not always ensure convergence to an unique solution for every case, the proposed method always guarantee fast convergence to accurate solution for each and every case. Therefore this non-invasive FFR estimation with the PBA is found to be a promising procedure for clinical patient-specific diagnosis of coronary stenosis, which is much simpler and more efficient than the traditional Windkessel circuit analogy approach. Our analysis also suggests that the proposed PBA combined with an efficient CFD solver can be used as a low cost, efficient and accurate method for patient-specific CAD diagnosis that could potentially serve as an alternative to the costly and harmful invasive coronary angiography (ICA) procedure. Future work on using the PBA for pulsatile flows in CATs with fluid structure interaction is suggested.

Acknowledgments: The authors would like to acknowledge the assistance and supply of the NT209, CT14 and CHN03 models by Dr. Zhong Liang as reported in [13]. This work was carried out with the support from Grant Award Number 110119FD4526 under "Clustering and Settling of Inertial Particles: Fluid-Structure Interaction Approach" project from Nazarbayev University awarded to Dr Sholpan Sumbekova.

Conflicts of Interest: All authors must disclose any financial and personal relationships with other people or organisations that could inappropriately influence (bias) their work. Examples of potential conflicts of interest include employment, consultancies, stock ownership, honoraria, paid expert testimony, patent applications/registrations, and grants or other funding.

Ethical Approval: was given by the IREC Committee of Nazarbayev University.

 doi:10.20944/preprints202301.0276.v1

References

1. Gersh Bernard J 2000. *Mayo Clinic Heart Book.* New York: William Morrow. pp. 6–8. ISBN 0-688-17642-9.
2. World Health Organization. 2018. *World Health Organization - Noncommunicable Diseases (NCD) Country Profiles, 2018.* https://www.who.int/nmh/countries/kaz_en.pdf?ua=1.
3. Roger V L et al. 2011. *Heart Disease and Stroke Statistics—2011 Update*. Circulation 123 (4). Ovid Technologies (Wolters Kluwer Health). doi:10.1161/cir.0b013e3182009701.
4. Meijboom W B et al. 2008. Diagnostic Accuracy of 64-Slice Computed Tomography Coronary Angiography. *Journal of the American College of Cardiology* 52 (25): 2135-2144. Elsevier BV. doi:10.1016/j.jacc.2008.08.058.
5. Spaan J A, Piek J J, Hoffman J I, and Siebes M 2006. "Physiological Basis of Clinically Used Coronary Hemodynamic Indices". *Circulation* 113 (3): 446-455. Ovid Technologies (Wolters Kluwer Health). doi:10.1161/circulationaha.105.587196.
6. Pijls Nico H J and Sels Jan-Willem E M 2012. "Functional Measurement of Coronary Stenosis". *Journal of the American College of Cardiology* 59 (12): 1045-1057. Elsevier BV. doi:10.1016/j.jacc.2011.09.077.
7. Puymirat E, Peace A, Mangiacapra F, Conte M, Ntarladimas Y, Bartunek J, Vanderheyden M, Wijns W, De Bruyne B, and Barbato E 2012. "Long-Term Clinical Outcome After Fractional Flow Reserve–Guided Percutaneous Coronary Revascularization in Patients With Small-Vessel Disease". *Circulation: Cardiovascular Interventions* 5 (1): 62-68. Ovid Technologies (Wolters Kluwer Health). doi:10.1161/circinterventions.111.966937.
8. Pijls N H, De Bruyne B, Peels K, Van Der Voort P H, Bonnier H J, Bartunek J, and Koolen J J 1996. Measurement of fractional flow reserve to assess the functional severity of coronary-artery stenoses. *New England Journal of Medicine*, 334(26), 1703-1708.
9. De Bruyne B et al. 2012. "Fractional Flow Reserve–Guided PCI versus Medical Therapy in Stable Coronary Disease". *New England Journal of Medicine* 367 (11): 991-1001. Massachusetts Medical Society. doi:10.1056/nejmoa1205361.
10. Secchi F et al. 2016. Fractional flow reserve based on computed tomography: an overview. *European Heart Journal Supplements* 2016 18 (Supplement E), E49–E56,doi:10.1093/eurheartj/suw014.
11.
12. Nørgaard B L et al. 2014. Diagnostic performance of noninvasive fractional flow reserve derived from coronary computed tomography angiography in suspected coronary artery disease: the NXT trial (Analysis of Coronary Blood Flow Using CT Angiography: Next Steps). *Journal of the American College of Cardiology*, 63(12), 1145-1155.
13. Zhong L, Zhang J M, Su B, San Tan R, Allen J C, and Kassab G S 2018. Application of patient-specific computational fluid dynamics in coronary and intra-cardiac flow simulations: Challenges and opportunities. *Frontiers in physiology*, 9.
14. Kim H J, Vignon-Clementel I E, Coogan J S, Figueroa C A, Jansen K E, and Taylor C A 2010. Patient-specific modeling of blood flow and pressure in human coronary arteries. *Annals of biomedical engineering*, 38(10), 3195-3209.
15. Murray C D 1926. The Physiological Principle of Minimum Work: I. The Vascular System and the Cost of Blood Volume. *Proceedings of the National Academy of Sciences of the United States of America*. 12 (3): 207–214. doi:10.1073/pnas.12.3.207. PMC 1084489. PMID 16576980
16. Updegrove A, Wilson, N M, Merkow, J, Lan, H, Marsden, A. L, & Shadden, S C. 2017. SimVascular: an open source pipeline for cardiovascular simulation. Annals of biomedical engineering, 45(3), 525-541.
17. Zhang J M et al. 2016. "Simplified Models of Non-Invasive Fractional Flow Reserve Based on CT Images". PLOS ONE 11 (5): e0153070. *Public Library of Science (PLoS)*. doi:10.1371/journal.pone.0153070.
18. Patankar, S. V. (1980). Numerical Heat Transfer and Fluid Flow. Taylor & Francis. ISBN 978-0-89116-522-4.